Journal of the American Heart Association

ORIGINAL RESEARCH

Virtual Transcatheter Interventions for Peripheral Pulmonary Artery Stenosis in Williams and Alagille Syndromes

Ingrid S. Lan, MS; Weiguang Yang, PhD; Jeffrey A. Feinstein, MD; Jacqueline Kreutzer, MD; R. Thomas Collins, II, MD; Michael Ma, MD; Gregory T. Adamson, MD; Alison L. Marsden, PhD

BACKGROUND: Despite favorable outcomes of surgical pulmonary artery (PA) reconstruction, isolated proximal stenting of the central PAs is common clinical practice for patients with peripheral PA stenosis in association with Williams and Alagille syndromes. Given the technical challenges of PA reconstruction and the morbidities associated with transcatheter interventions, the hemodynamic consequences of all treatment strategies must be rigorously assessed. Our study aims to model, assess, and predict hemodynamic outcomes of transcatheter interventions in these patients.

METHODS AND RESULTS: Isolated proximal and "extensive" interventions (stenting and/or balloon angioplasty of proximal and lobar vessels) were performed in silico on 6 patient-specific PA models. Autoregulatory adaptation of the cardiac output and downstream arterial resistance was modeled in response to intervention-induced hemodynamic perturbations. Postintervention computational fluid dynamics predictions were validated in 2 stented patients and quantitatively assessed in 4 surgical patients. Our computational methods accurately predicted postinterventional PA pressures, the primary indicators of success for treatment of peripheral PA stenosis. Proximal and extensive treatment achieved median reductions of 14% and 40% in main PA systolic pressure, 27% and 56% in pulmonary vascular resistance, and 10% and 45% in right ventricular stroke work, respectively.

CONCLUSIONS: In patients with Williams and Alagille syndromes, extensive transcatheter intervention is required to sufficiently reduce PA pressures and right ventricular stroke work. Transcatheter therapy was shown to be ineffective for long-segment stenosis and pales hemodynamically in comparison with published outcomes of surgical reconstruction. Regardless of the chosen strategy, a virtual treatment planning platform could identify lesions most critical for optimizing right ventricular afterload.

Key Words: computational fluid dynamics ■ peripheral pulmonary artery stenosis ■ pulmonary artery reconstruction ■ pulmonary artery stenting ■ pulmonary hemodynamics

Complex pulmonary artery (PA) stenoses, whether in isolation or in combination with additional congenital heart defects, present challenges in both diagnostic and treatment strategies. In patients with Williams syndrome (WS) and Alagille syndrome (AS), the associated peripheral PA stenosis (PPAS) generally yields severe hemodynamic abnormalities. In previous studies, we have shown surgical PA reconstruction to effectively normalize right ventricular (RV) pressure and provide excellent long-term outcomes with low rates of morbidity, mortality, and reintervention for the vast majority of patients.[1,2] We recognize, however, that patch augmentation of lobar and segmental PA stenoses is a challenging surgery requiring long hours of cardiopulmonary bypass and specialized expertise not universally available. Surgical, transcatheter, or hybrid approaches addressing only the most proximal central PAs thus remain the standard of care at most centers

Correspondence to: Alison L. Marsden, PhD, Clark Center E1.3, 318 Campus Drive, Stanford, CA, USA. E-mail: amarsden@stanford.edu

Supplemental Material for this article is available at https://www.ahajournals.org/doi/suppl/10.1161/JAHA.121.023532

For Sources of Funding and Disclosures, see page 10.

JAHA is available at: www.ahajournals.org/journal/jaha

CLINICAL PERSPECTIVE

What Is New?

- Isolated proximal stenting is insufficient for peripheral pulmonary artery (PA) stenosis in patients with Williams and Alagille syndromes.
- Extensive stenting and/or angioplasty can decrease PA pressures to half systemic levels in cases without long-segment stenosis, but these improvements still pale in comparison with published surgical outcomes.
- We have engineered a spatial resistance "map" allowing clinicians to easily assess the clinical import of stenoses.

What Are the Clinical Implications?

- Surgical PA reconstruction remains the preferred strategy for multilevel PA stenoses in Williams and Alagille syndromes, but if transcatheter interventions are pursued out of necessity regarding certain associated morbidities or unavailability of surgical expertise, then extensive stenting and/or angioplasty should be performed to achieve adequate acute hemodynamic outcomes.
- Computational fluid dynamics presents a promising future for furthering our understanding of the complex peripheral PA stenosis scenario via virtual patient-specific treatment planning.

Nonstandard Abbreviations and Acronyms

AS	Alagille syndrome
CFD	computational fluid dynamics
CTA	computed tomography angiography
LPA	left pulmonary artery
MPA	main pulmonary artery
PPAS	peripheral pulmonary artery stenosis
RPA	right pulmonary artery
RVSW	right ventricular stroke work
WS	Williams syndrome

despite suboptimal clinical and procedural outcomes, including significant residual disease, persistent RV hypertension, pulmonary hemorrhage, vessel dissection, aneurysm formation, PA rupture, in-stent restenosis, and even death.[3–7] Given these unfavorable results and the technical challenges associated with surgical PA reconstruction, there is a pressing need to better understand the hemodynamics associated with various transcatheter approaches and to further develop a virtual treatment planning platform to identify lesions most critical for optimizing RV afterload/pulmonary vascular resistance (PVR; at the macro level) and thus PA and RV pressures.

Image-based computational fluid dynamics (CFD) offers a unique framework for performing and evaluating virtual interventions on a patient-specific basis. Accurate predictions of postinterventional hemodynamics are critical to the success of a virtual treatment planning platform and thus must incorporate the relevant physiology, including blood flow autoregulation. Although prior studies have modeled coronary autoregulation,[8,9] most CFD studies investigating postinterventional PA hemodynamics have employed the nonphysiological assumption that the downstream resistance remains unchanged.[9–11] Yang et al previously performed virtual PA reconstruction for patients with AS and achieved accurate predictions of postoperative PA flow splits via adaptive outflow boundary conditions.[12,13] Nonetheless, accurate predictions of postoperative proximal PA pressures, the primary indicators of success in PPAS treatment, remained elusive with discrepancies up to 18 mm Hg.[12] Furthermore, adaptation of the downstream resistance was modeled in response to wall shear stress only, with no consideration of the counteracting myogenic and metabolic responses necessary for stable adaptation.[14–17]

To our knowledge, no prior CFD studies have investigated hemodynamic conditions following transcatheter interventions in patients with WS or AS. In this study, we aim to accurately predict postinterventional PA hemodynamics for patients with PPAS in association with WS and AS using physiologically sound methods to adapt both the cardiac output and downstream pulmonary resistance. We validate our methods on 2 stented patients and subsequently assess the hemodynamic consequences of transcatheter therapy in 4 surgical patients. We further build the foundations of a virtual treatment planning platform by identifying lesions most responsible for the elevated PVR. Finally, we develop preliminary clinical recommendations for PPAS based on controlled comparisons of different transcatheter strategies within the same patient cohort. Our methods are broadly applicable to other CFD investigations of virtual interventions in congenital heart disease.

METHODS

Patient Cohort Identification

Under a protocol approved by the Stanford Institutional Review Board, patients with PPAS in association with WS and AS in the Lucile Packard database were retrospectively categorized as having undergone either PA stenting or surgical reconstruction. For validation of postinterventional hemodynamic predictions, inclusion criteria for the stenting cohort required both prestent and poststent PA pressures from cardiac

catheterization. In addition, either a prestent computed tomography angiography (CTA) or magnetic resonance angiography (MRA) or the combination of a poststent CTA/MRA alongside detailed cardiac catheterization angiograms was required for anatomical modeling. Inclusion criteria for the surgical cohort required only a preoperative CTA/MRA and preoperative PA pressures from cardiac catheterization. Lung perfusion scans, although not routinely performed for these patients and not required for either cohort, were collected if available. No informed consent was required for this retrospective clinical data collection. All data supporting the findings of this study are available from the corresponding author upon reasonable request.

Patient-Specific Model Construction

Patient-specific preinterventional 3-dimensional anatomical models of the PA tree were constructed from CTA/MRA in SimVascular[18] by creating pathlines and lumen segmentations along the PAs and subsequently lofting the segmentations. For patients in the stenting cohort with poststent CTA/MRA only, models were first constructed from the poststent scans. Then, referencing the catheterization angiograms under the guidance of interventional cardiologists, we virtually modified the central left PA (LPA) and right PA (RPA) segmentations to reflect the prestent anatomy. The main PA (MPA), beginning immediately distal to the pulmonary valve, as well as all lobar, segmental, and subsegmental vessels were modeled.

Postinterventional models were constructed via virtual transcatheter repair of the preinterventional models, again by modifying lumen segmentations to achieve desired stent diameters and lengths. We performed 2 virtual procedures for each patient: (1) a proximal procedure involving stenting of only the LPA and RPA and (2) an extensive procedure involving proximal stenting alongside additional stenting and/or balloon angioplasty of more distal lobar vessels. Under the guidance of 2 interventional cardiologists, decisions regarding the number and position of the stent(s), whether to "jail" a vessel, and the choice of stent versus balloon angioplasty in the more distal lesions were made based on in vivo hemodynamics, their extensive experience in transcatheter treatment of these complex populations, and an assumed availability of the necessary technical expertise. All jailed side branches underwent virtual balloon angioplasty, as would commonly be performed during the procedure.

All anatomical models were meshed in MeshSim (Simmetrix Inc.) with 3 boundary layers. Based on a mesh convergence study, meshes with 1.7 to 1.9 million linear tetrahedral elements were selected to ensure convergence of pressures and flows at the MPA, RPA, LPA, and all outlets.

Fluid–Structure Interaction Simulation

Hemodynamic simulations were performed with svSolver, SimVascular's finite element solver[19–21] for fluid–structure interaction between an incompressible, Newtonian fluid and a linear elastic membrane for the vascular wall[22,23] (see Data S1 for details). We prescribed a vessel wall thickness of 10% of the diameter at every inlet and outlet and a smoothly varying thickness distribution over the remainder of the wall. For preinterventional simulations, the Young's modulus was uniformly prescribed as 2.5×10^6 dyn/cm^2 based on mechanical characterization of healthy murine PAs[24] and healthy and hypertensive adult human PAs[25,26]; stented regions were prescribed 2.5×10^8 dyn/cm^2.

The MPA inlet and PA outlets were coupled to 0-dimensional lumped parameter networks[27] representing the upstream right heart[26,28–30] (see Data S1 for details) and downstream vasculature, respectively (Figure 1A). Each PA outlet was coupled to 3 RCR Windkessel models in series, corresponding to the downstream arterial, capillary, and venous compartments, with the pulmonary capillary wedge pressure assigned as the constant left atrial pressure. The cardiac output[31] and PA outlet pressures were prescribed as Dirichlet and Neumann boundary conditions, respectively.

All simulations were run for 6 cardiac cycles to ensure convergence to a limit cycle; only the final cycle was analyzed. For each patient, right heart parameters were unchanged from preintervention to postintervention, as the governing ordinary differential equations inherently adapt the cardiac output under altered PA pressures.[32] Arterial resistances downstream of the PA outlets were adapted with an empirical model for stable microvascular autoregulation,[15,16] as discussed below in Autoregulatory Microvascular Adaptation.

Automated Tuning of Preinterventional Boundary Conditions

Systolic, diastolic, and mean MPA, RPA, and LPA pressures were used as our patient-specific clinical targets. The RPA and LPA pressures used were the central RPA and LPA pressures measured between the ostium and the corresponding upper lobe branch takeoff. In our simulations, MPA pressures were assessed at model inlets, and RPA and LPA pressures were assessed at slices consistent with the locations of the catheterization-derived measurements. To accelerate the simulation pipeline, we developed an automated tuning framework[33] for identifying boundary conditions that best achieve these target pressures. Our framework leveraged a high-fidelity 0-dimensional surrogate[34,35] of the 3-dimensional finite element PA domain (Figure 1B), in which Bernoulli-type resistors accurately captured the nonlinear flow in the diseased anatomies.

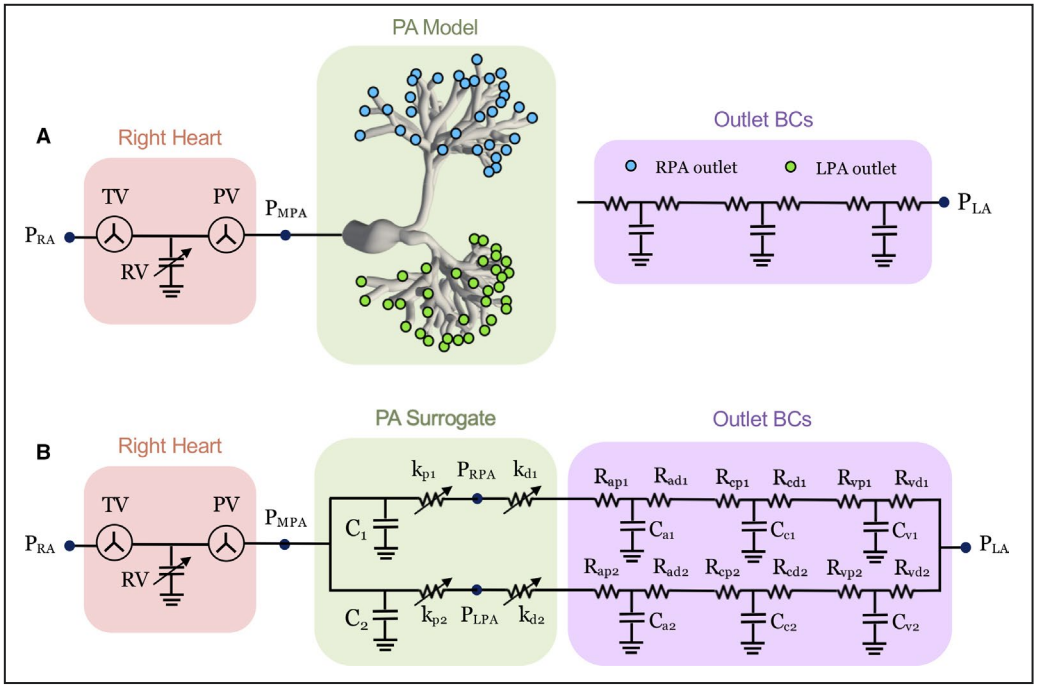

Figure 1. Automated tuning of preinterventional boundary conditions.
A, The main pulmonary artery (MPA) inlet is coupled to a right heart network consisting of a constant right atrial (RA) pressure (P_{RA}), tricuspid valve (TV), right ventricle (RV), and pulmonary valve (PV). Each outlet is coupled to 3 RCR Windkessel models in series, corresponding to the arterial, capillary, and venous compartments, with a constant left atrial (LA) pressure (P_{LA}). **B**, For tuning of patient-specific boundary conditions (BCs), the PA model is reduced to a 0-dimensional surrogate, and the outlet BCs are bilaterally aggregated. LPA indicates left pulmonary artery; PA, pulmonary artery; RPA, right pulmonary artery; P_{LPA}, LPA pressure, P_{MPA}, MPA pressure; and P_{RPA}, RPA pressure. All C's indicate capacitances, k's indicate coefficients for Bernoulli-type resistors, and R's indicate resistances. Subscripts 1 and 2 indicate aggregated parameters for the right and left trees, respectively. Subscripts a, c, and v indicate arterial, capillary, and venous parameters. Subscripts p and d indicate proximal and distal parameters.

In each tuning iteration, this low-cost surrogate was coupled to optimization algorithms[36] (see Data S1 for details), and newly optimized boundary conditions were prescribed in the subsequent simulation.

Autoregulatory Microvascular Adaptation

Beyond cardiac output adaptation, blood flow autoregulation involves adaptation of the microvascular resistance in response to hemodynamic perturbations, such as those induced by cardiovascular interventions. Although we adopted a similar approach to Yang et al[12,13] involving structured tree[37–40] representations of the downstream vasculature, we limited this representation to the small arteries and arterioles for which structured trees were originally developed. Furthermore, we considered adaptation in response to perturbations in intraluminal pressure and metabolite concentrations in addition to wall shear stress. These myogenic and metabolic[41] responses have been shown to counteract the wall shear stress–dependent response and produce stable networks, realistic distributions of vessel diameters, and physiological hemodynamics.[14–17] Indeed, as Yang et al[12] noted, multiple rounds of solely wall shear stress–based adaptation could yield nonphysiological predictions of monotonically increasing flow to the lung undergoing obstruction relief. We therefore implemented an empirical model developed by Pries et al[15,16] to describe their experimental observations of topology and anatomy in rat mesentery microvasculature. To adapt this model to PA microvasculature, we leveraged numerical optimization to identify model parameters yielding the most stable networks under adaptation with preinterventional hemodynamics (see Data S1 for details). The resistance of each adapted tree was then prescribed as the adapted downstream arterial resistance for the postinterventional simulation.

Computation of Resistances and RV Stroke Work

To compute resistances from simulated hemodynamics in the 3-dimensional PA domain, the tree

topology was first determined using the Vascular Modeling Toolkit.[42] Vessel centerlines were clipped into segments between successive branching regions. Spatially and temporally averaged pressures and temporally averaged volumetric flow rates were extracted at cross-sectional slices 75% down the lengths of all segments to avoid ill-defined slices in branching regions. Segment resistances were computed assuming Poiseuille flow and projected onto vessel centerlines.

For each simulation, the 3-dimensional and total PVR were computed. This "total PVR" included contributions from both the 3-dimensional segment resistances and prescribed 0-dimensional Windkessel resistances. The 0-dimensional resistances were first added to the corresponding 3-dimensional outlet segment resistances, which were then topologically propagated upstream to the MPA inlet. The 3-dimensional PVR was instead computed without consideration of 0-dimensional resistances. All segment and aggregate resistances were indexed by patient body surface areas (BSAs) to facilitate comparisons across age. The RV stroke work (RVSW) was computed as the integral over the RV pressure-volume loop and indexed by BSA.

Statistical Analysis

Results were presented by their median and interquartile range (IQR), and all statistical testing was performed in R (version 3.6.3) to detect significance at α=0.05. The Friedman test was first performed to detect significant hemodynamic differences across the preinterventional, proximal intervention, and extensive intervention conditions. In cases where significant differences were detected, we subsequently identified the significantly different pairs via pairwise Wilcoxon signed-rank tests with the Bonferroni correction for multiple testing.

RESULTS

Anatomical Modeling

A total of 6 patients with WS (n=2) and AS (n=4) were included: 2 in the stenting validation cohort (AS-1, AS-2) and 4 in the surgical cohort (AS-3, AS-4, WS-1, WS-2; Table). AS-2 was the only patient for whom we collected a postinterventional imaging scan in lieu of a preinterventional scan. An average of 93 outlets (range, 72–105) were modeled (Figure 2). The median MPA, RPA, and LPA diameters were 1.3 cm (IQR, 1.1–1.8 cm), 0.53 cm (IQR, 0.40–0.68 cm), and 0.40 cm (IQR, 0.34–0.56 cm), respectively. Among the stenting cohort, the extensive intervention in patient AS-1 and proximal intervention in patient AS-2 were procedures actually performed and used for validation of our postinterventional hemodynamic predictions.

Automated Tuning Framework

For each patient, up to 3 simulations were required to achieve preinterventional systolic, diastolic, and mean MPA, RPA, and LPA target pressures within 5 mm Hg (Table S1). Although PA flow splits were not uniformly available and thus excluded from tuning targets, the simulated RPA flow fractions exhibited only 1% to 3% discrepancies for the 3 patients with available data. These results suggest that our computational methods can accurately determine bulk RPA/LPA flow splits from the routinely collected clinical data without the need for lung perfusion scans.

Autoregulatory Physiology

In all virtual interventions, the cardiac output uniformly increased (Figure 3A) in response to the reduced PVR

Table. Baseline Patient Characteristics

Patient	Sex	Age, y	BSA (m^2)	P_{MPA} (mm Hg), systolic/diastolic	CI (L/min per m^2)	Flow split, percentage right	Comorbidities
AS-1	Female	16.8	1.39	90/18; mean, 42	4.20	52	Stage IV CKD, cholestasis, cirrhosis, exocrine pancreatic insufficiency, systemic hypertension
AS-2	Male	0.35	0.25	100/6; mean, N/A	4.28	N/A	Tetralogy of Fallot, PAPVR, cholestasis, cirrhosis, bronchomalacia, single coronary artery
AS-3	Male	13.2	1.00	68/15; mean, 38	2.60	68	Cholestasis
AS-4	Male	5.80	0.64	50/11; mean, 26	4.20	56	Cholestasis, celiac artery stenosis
WS-1	Male	0.63	0.34	125/21; mean, N/A	3.59	N/A	Supravalvar aortic stenosis, renal artery stenosis, bronchomalacia
WS-2	Female	0.20	0.25	93/16; mean, 42	4.08	N/A	Supravalvar aortic stenosis

AS indicates Alagille syndrome; BSA, body surface area; CI, cardiac index; CKD, chronic kidney disease; N/A, not available; PAPVR, partial anomalous pulmonary venous return; P_{MPA}, main pulmonary artery pressure; and WS, Williams syndrome.

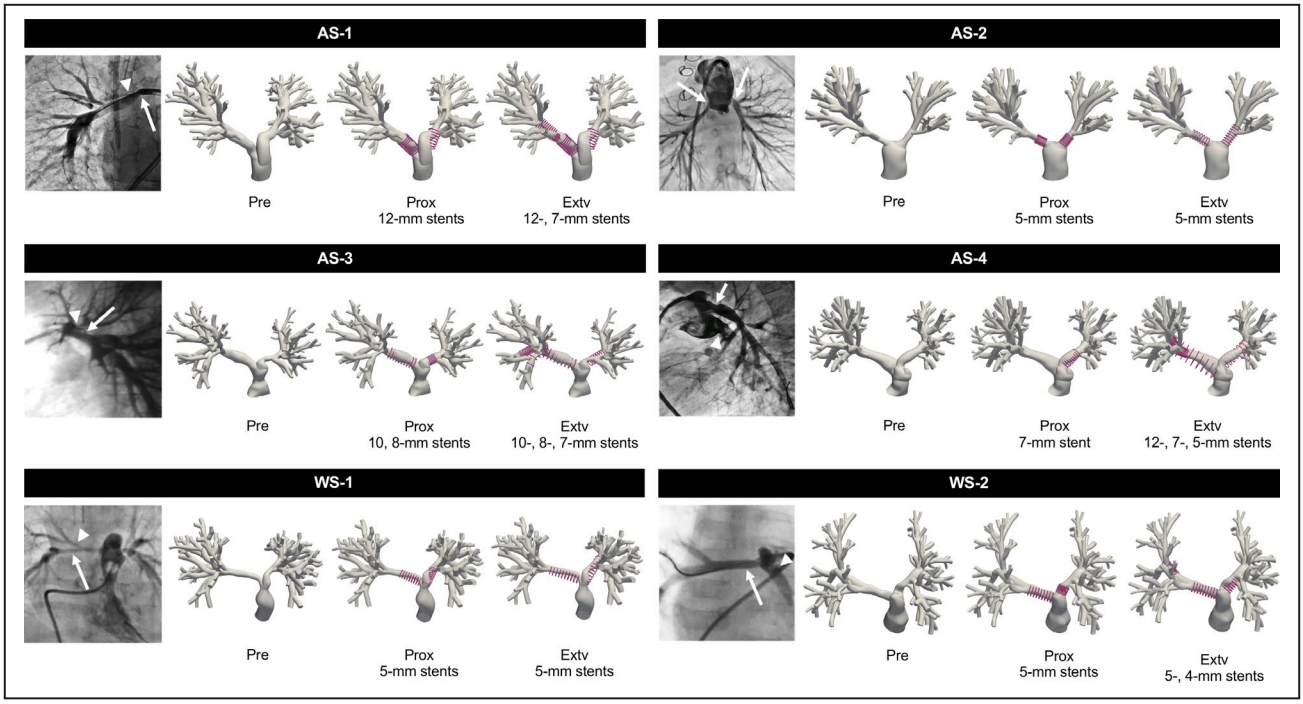

Figure 2. Virtual proximal and extensive transcatheter interventions.
Catheterization angiograms indicating representative lesions, the image-based preinterventional models, and modified segmentations for virtual repair. Stent diameters are annotated. AS indicates Alagille syndrome; Extv, extensive intervention; Pre, preintervention; Prox, proximal intervention; and WS, Williams syndrome.

as a result of obstruction relief.[43] Further increases in cardiac output were observed upon extensive repair.

Human PPAS-specific microvascular adaptation parameters identified via numerical optimization are documented in Data S1. Microvascular adaptation uniformly decreased the downstream arterial resistance for all proximal (median, 5.18%) and extensive (median, 17.5%) procedures, yielding further increases in cardiac output as a consequence of the right heart model (Figure 3B). These changes to the downstream resistance were negligible compared with the intervention-induced changes to the 3-dimensional resistance. Microvascular adaptation yielded similarly negligible effects on the PA flow split, with a maximum change of 3% in the RPA flow.

Postinterventional Hemodynamics

Using the available clinical data, we successfully validated our predictions of systolic, diastolic, and mean MPA, RPA, and LPA pressures within 5 mm Hg for the extensive intervention in AS-1 and proximal intervention in AS-2 (Table S1). Whereas proximal intervention alone reduced the systolic and mean MPA pressures, respectively, by 14% (IQR, 4.36%–25.3%) and 11% (IQR, 3.19%–16.9%), extensive intervention achieved respective reductions of 40% (IQR, 32.9%–41.1%) and 24% (IQR, 20.9%–28.1%; Figure 4A). Of note, patients AS-1 and AS-4 did not benefit from proximal intervention alone and required extensive repair of their predominantly distal lesions. The systolic MPA pressure in patient WS-1 remained hypertensive at 114 mm Hg despite extensive intervention (Figure 5).

Proximal intervention led to diminished pressure gradients across the central PAs and increased RPA and LPA pressures. With further PVR reductions (Figure 4B) by way of extensive repair, MPA and branch PA pressures decreased.

A comparison of the BSA-indexed 3-dimensional and total PVR revealed that the elevated resistances in these patients were predominantly driven by PA lesions rather than the downstream microvasculature. Whereas proximal intervention reduced the BSA-indexed PVR and RVSW, respectively, by 27% (IQR, 7.81%–37.6%) and 10% (IQR, 1.07%–21.5%), extensive intervention achieved larger reductions of 56% (IQR, 41.5%–63.0%) and 45% (IQR, 30.9%–50.9%), respectively. We again observed the lack of improvement experienced by patients AS-1 and AS-4 upon proximal intervention. Furthermore, although patient WS-1 experienced a 20% reduction in BSA-indexed PVR from proximal intervention and an additional 7% reduction from extensive intervention, the autoregulatory increase in cardiac output yielded only minor improvements in MPA pressure and effectively no changes to the BSA-indexed RVSW.

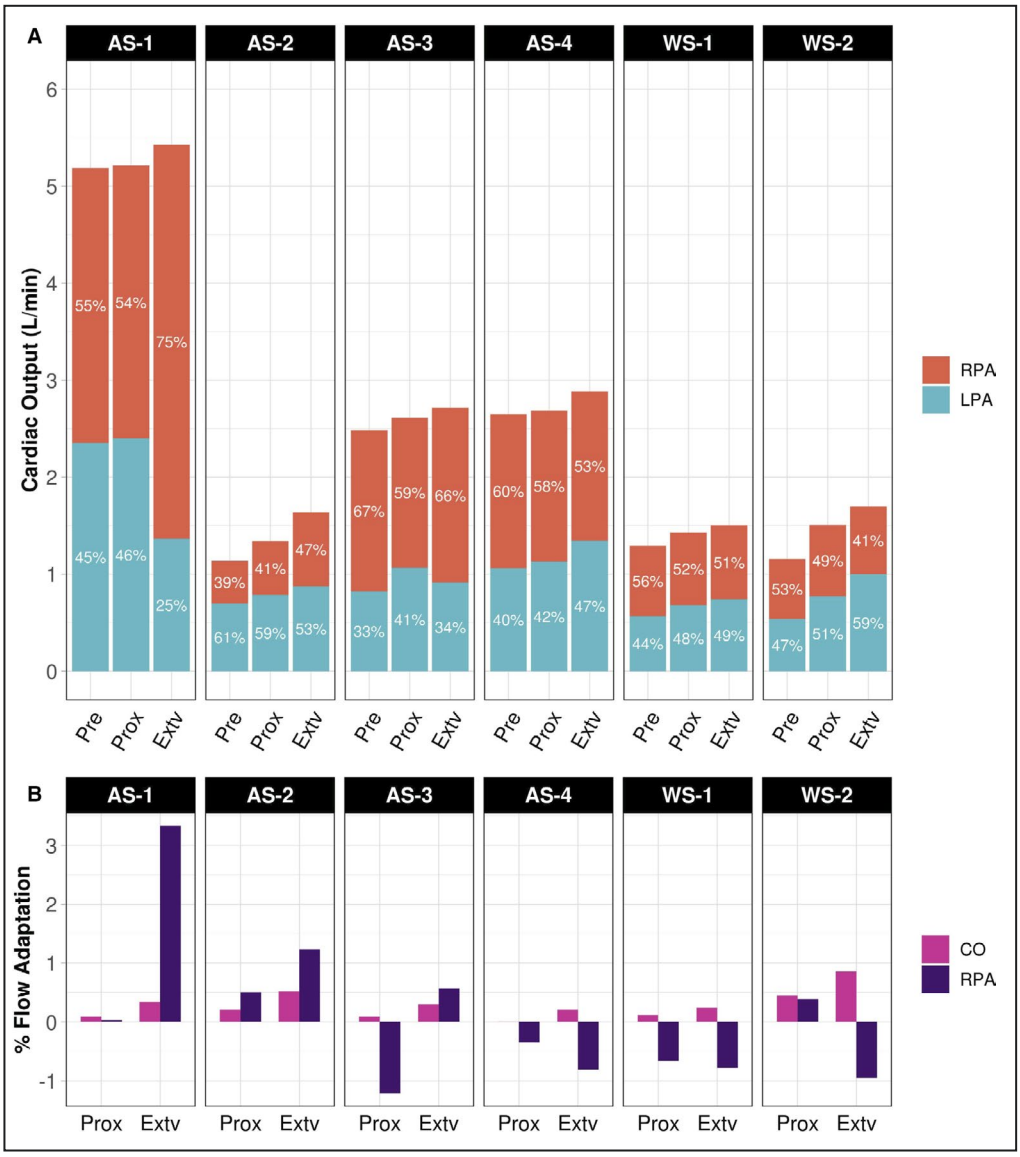

Figure 3. Autoregulatory adaptation of the cardiac output and downstream arterial resistance. **A**, Simulated CO (L/min) and central RPA/LPA flow splits (annotated). **B**, Negligible percent changes in CO and time-averaged RPA flow attributed to downstream microvascular adaptation. AS indicates Alagille syndrome; CO, cardiac output; Extv, extensive intervention; LPA, left pulmonary artery; Pre, preintervention; Prox, proximal intervention; RPA, right pulmonary artery; and WS, Williams syndrome.

Segment Resistances for Treatment Planning

In addition to providing accurate posttreatment hemodynamic predictions, a PPAS treatment planning platform must identify lesions most critical for normalizing PVR and thus PA and RV pressures. Visualization of segment resistances on vessel centerlines (Figure 6) enables both cardiothoracic surgeons and interventional cardiologists to accurately identify resistance hotspots. Although several distal stenoses were virtually repaired in our extensive interventions, further hemodynamic improvements could be gained upon addressing the remaining lesions.

DISCUSSION

Our study represents the first to accurately model the severely nonlinear and hypertensive hemodynamics of PPAS in WS and AS and to further predict postinterventional pressures, the primary indicators of success in PPAS repair. Novel aspects include (1) an automated tuning framework that leverages a high-fidelity, 0-dimensional surrogate and numerical optimization to efficiently identify boundary conditions that achieve clinically measured PA pressures and flow splits, (2) autoregulatory adaptation of the cardiac output and microvascular resistance in response

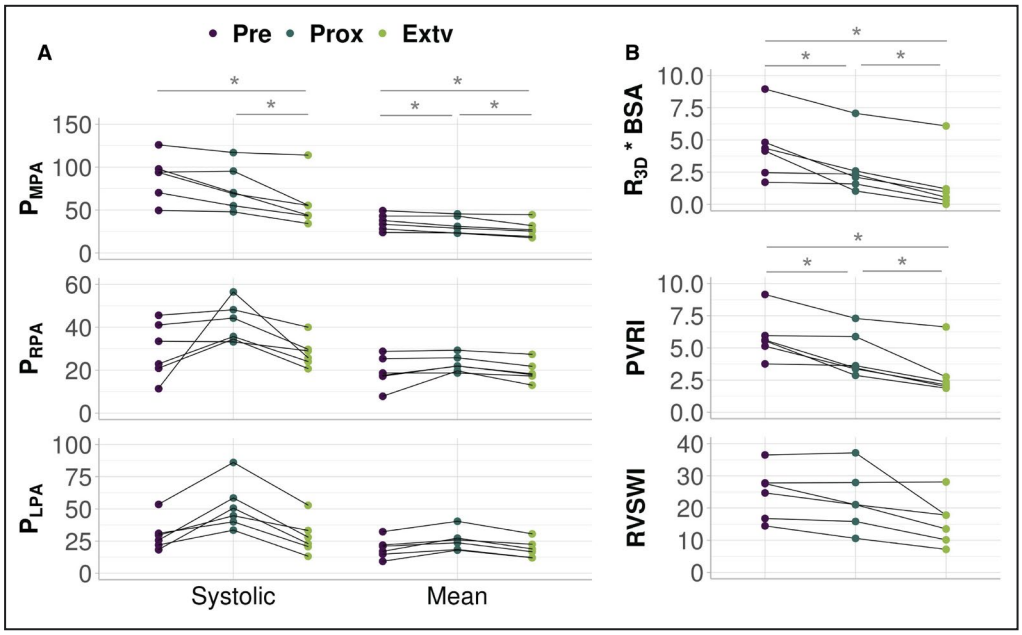

Figure 4. Simulated preinterventional and postinterventional hemodynamics (n=6).
A, Simulated main, central right, and central left pulmonary artery (MPA, RPA, LPA) systolic and mean pressures (mm Hg). Line segments denote data from the same patient. **B**, Simulated body surface area (BSA)–indexed 3-dimensional resistance (R_{3D}xBSA), total pulmonary vascular resistance (PVRI; Wood units·m^2), and right ventricular stroke work (RVSWI; cJ/m^2). *P<0.05 with the Bonferroni correction. Extv indicates extensive intervention; Pre, preintervention; Prox, proximal intervention; P_{LPA}, LPA pressure; P_{MPA}, MPA pressure; and P_{RPA}, RPA pressure.

to intervention-induced hemodynamic perturbations, (3) development of a new resistance "map" allowing clinicians to easily determine the clinical import of stenoses, and (4) a controlled hemodynamic comparison between proximal and extensive transcatheter interventions in the same patient cohort.

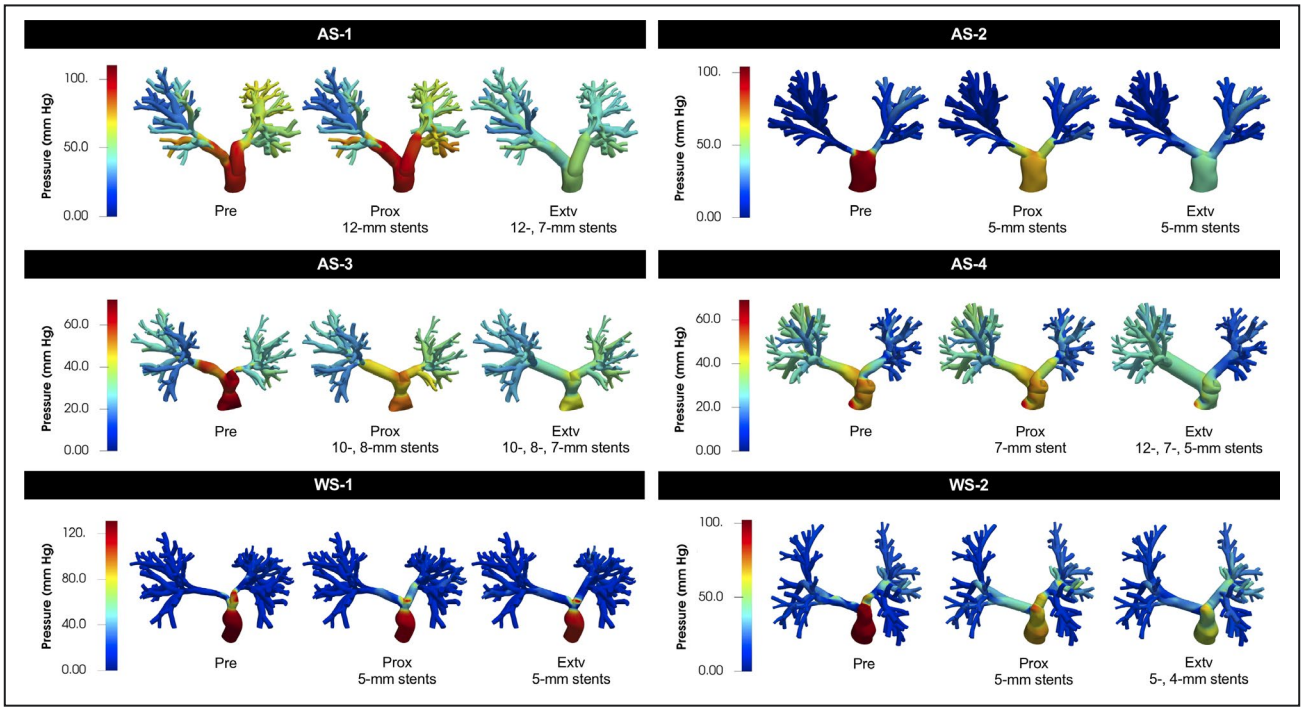

Figure 5. Simulated preinterventional and postinterventional systolic pressure distributions at peak systole.
Stent diameters are annotated. AS indicates Alagille syndrome; Extv, extensive intervention; Pre, preintervention; Prox, proximal intervention; and WS, Williams syndrome.

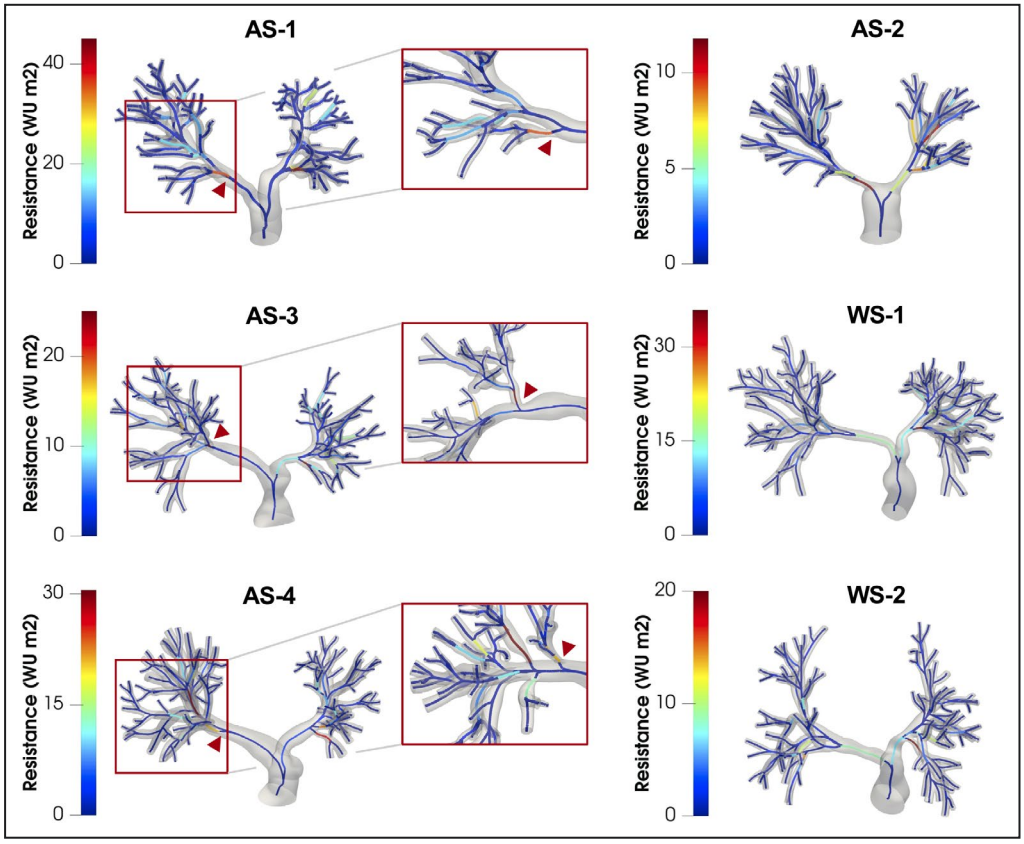

Figure 6. Preinterventional vessel segment resistances projected onto vessel centerlines. Regions with severe distal pulmonary artery lesions are highlighted and rotated for ease of display. AS indicates Alagille syndrome; WS, Williams syndrome; and WU, Wood units.

Although we observed negligible effects of microvascular adaptation on the postinterventional cardiac output and PVR in our cohort, this observation may not extend to other interventions or patients with lower 3-dimensional resistances, such as patients with univentricular heart undergoing the Fontan procedure.[32]

As the optimal treatment strategy for WS and AS continues to be debated among centers advocating either surgical PA reconstruction or transcatheter interventions, our study offers insight into the range of potential transcatheter outcomes. In practice, each balloon angioplasty is associated with some probability of acute success in the catheterization laboratory. The proximal intervention presented here, in which stenting is performed only on the central PAs and all balloon angioplasties are unsuccessful, can therefore be considered the worst-case scenario for these patients. The extensive intervention, in which distal PAs are additionally stented and all balloon angioplasties are successful, can be considered the best-case scenario.

Proximal Stenting Alone Is Insufficient for Patients With WS and AS

We have shown that the most common clinical practice of stenting only the central PAs, that is, the proximal intervention, confers minimal benefits on patients with distal lesions. Cunningham et al previously reported a modest decrease of the median systolic RV:aortic pressure ratio from 1.0 to 0.88.[5] These combined results suggest that in complex PPAS, especially when associated with WS or AS, proximal stenting alone is insufficient and should be avoided.

Surgical Reconstruction Achieves Larger Hemodynamic Improvements Than Extensive Transcatheter Therapy

In our study, extensive interventions reduced the median systolic MPA pressure (94.0 to 49.6 mm Hg) by 47%. Although impressive, this was a much smaller improvement than reported in the surgical literature for patients with WS (66% reduction; 80 to 27 mm Hg)[1] and AS (61% reduction; 75 to 29 mm Hg).[2] In addition, these surgical results were reported to persist at long-term follow-ups of 1.5 and 2.5 years, respectively. WS and AS, however, have been associated with significantly worse odds for sustained increases in intraluminal diameters following transcatheter therapy.[4,7]

We present our data with some fear and trepidation, as one might incorrectly infer that we are recommending the use of extensive transcatheter interventions to

treat these patients with highly complex conditions. In our center, where we have decades of institutional experience with surgical reconstruction of complex PA stenoses and excellent long-term patient outcomes offered by the growth potential of homograft patches, surgical PA reconstruction is the preferred strategy. Most notably, even the "best-case" immediate postinterventional hemodynamic outcomes presented here may worsen over time with in-stent restenosis or as jailed vessels initially salvaged by balloon angioplasty become occluded over time. We do understand, however, that despite their generally inferior outcomes, transcatheter interventions may be necessary in certain circumstances, including the associated morbidities in WS and AS, or when treatment at a center with significant surgical experience is simply not an option. We in fact employed extensive transcatheter therapy as a bridge to liver transplantation for patient AS-1, who was too ill for surgical repair.

CFD Presents a Promising Future for Virtual PPAS Treatment Planning

Regardless of the chosen strategy, our spatial resistance "map" offers a promising foundation for a virtual PPAS treatment planning platform. We have demonstrated our ability to accurately model baseline hemodynamics and predict postinterventional hemodynamics with 3-dimensional CFD simulations. To provide real-time hemodynamic information on such a platform, however, additional validation is needed along with reduced-order model development to accelerate the simulation process while maintaining its predictive ability.

Study Limitations

Given the paucity of complete data sets necessary for tuning our image-based CFD simulations, our study was performed on a small cohort. Our stenting cohort size was further limited by the predominant surgical approach undertaken at our center. As lung perfusion scans are not routinely performed for these patients, only postinterventional PA pressure predictions were validated. Numerous hemodynamic confounding factors exist (including the effects of anesthesia, contrast, and catheter-induced tricuspid regurgitation) in the acquisition of catheterization data and, although important for data accuracy, were not considered at this time. In addition, patient-specific inflow waveforms were unavailable, which otherwise could have served as optimization targets for the right heart model.

Additional limitations include the lack of PA mechanical characterization for WS and AS and the use of a linear membrane model for the PA wall. We also did not consider genetic variability or any associated comorbidities.

Finally, although the variable success rates for balloon angioplasty were not addressed in this study, the statistical uncertainty could be propagated forward to simulated hemodynamic metrics using uncertainty quantification techniques.[44] Nonetheless, our study presents a fair assessment of the transcatheter strategy via evaluations of both worst-case and best-case scenarios.

CONCLUSIONS

Despite several retrospective reports of outcomes following either surgical PA reconstruction or transcatheter intervention in patients with PPAS in association with WS and AS, the standard of care continues to be debated. In this study, we engineered a resistance "map" allowing clinicians to easily assess the clinical import of stenoses and demonstrated the ability to accurately model and predict baseline and postinterventional hemodynamics using patient-specific, image-based CFD simulations. Controlled comparisons of different transcatheter interventions within the same cohort revealed that in the setting of complex PPAS, proximal stenting alone yields little benefit. In cases without long-segment stenosis, extensive interventions can reduce pressures to approximately half systemic levels. These hemodynamic improvements, however, still pale in comparison with reported surgical outcomes. Ultimately, the optimal treatment strategy must be chosen alongside consideration of other factors, including the availability of surgical expertise and the higher morbidity rates associated with transcatheter interventions. Computational modeling may guide patient-specific treatment planning to optimize hemodynamic outcomes while avoiding unnecessary procedures.

ARTICLE INFORMATION

Received August 5, 2021; accepted January 5, 2022.

Affiliations

Department of Bioengineering (I.S.L., J.A.F., A.L.M.); and Department of Pediatrics (Cardiology) (W.Y., J.A.F., R.T.C., G.T.A., A.L.M.), Stanford University, Stanford, CA; Department of Pediatrics (Cardiology), University of Pittsburgh, Pittsburgh, PA (J.K.); Department of Medicine (Cardiovascular Medicine) (R.T.C.); Department of Cardiothoracic Surgery (M.M.) and Institute for Computational and Mathematical Engineering, Stanford University, Stanford, CA (A.L.M.).

Sources of Funding

This work is supported by National Institutes of Health grant R01-EB018302 and the Vera Moulton Wall Center for Pulmonary Vascular Disease at Stanford University. I.S. Lan is supported by the National Science Foundation Graduate Research Fellowship and the Stanford Graduate Fellowship in Science and Engineering.

Disclosures

None.

Supplemental Material

Data S1
Table S1

REFERENCES

1. Collins RT II, Mainwaring RD, MacMillen KL, Hanley FL. Outcomes of pulmonary artery reconstruction in Williams syndrome. *Ann Thoracic Surg*. 2019;108:146–153. doi: 10.1016/j.athoracsur.2019.02.013
2. Luong R, Feinstein JA, Ma M, Ebel NH, Wise-Faberowski L, Zhang Y, Peng LF, Yarlagadda VV, Shek J, Hanley FL, et al. Outcomes in patients with Alagille syndrome and complex pulmonary artery disease. *J Pediatr*. 2021;229:86–94. doi: 10.1016/j.jpeds.2020.09.053
3. Adamson GT, Peng LF, Feinstein JA, Yarlagadda VV, Lin A, Wise-Faberowski L, McElhinney DB. Pulmonary hemorrhage in children with Alagille syndrome undergoing cardiac catheterization. *Catheter Cardiovasc Interv*. 2020;95:262–269. doi: 10.1002/ccd.28508
4. Hallbergson A, Lock JE, Marshall AC. Frequency and risk of in-stent stenosis following pulmonary artery stenting. *Am J Cardiol*. 2014;113:541–545. doi: 10.1016/j.amjcard.2013.10.016
5. Cunningham JW, McElhinney DB, Gauvreau K, Bergersen L, Lacro RV, Marshall AC, Smoot L, Lock JE. Outcomes after primary transcatheter therapy in infants and young children with severe bilateral peripheral pulmonary artery stenosis. *Circ Cardiovasc Interv*. 2013;6:460–467. doi: 10.1161/CIRCINTERVENTIONS.112.000061
6. Geggel RL, Gauvreau K, Lock JE. Balloon dilation angioplasty of peripheral pulmonary stenosis associated with Williams syndrome. *Circulation*. 2001;103:2165–2170. doi: 10.1161/01.CIR.103.17.2165
7. Cobb H, Spray B, Daily J, Dossey A, Angtuaco MJ. Cutting balloon angioplasty on branch pulmonary artery stenosis in pediatric patients. *Catheter Cardiovasc Interv*. 2021;98:526–532. doi: 10.1002/ccd.29803
8. Kim HJ, Jansen KE, Taylor CA. Incorporating autoregulatory mechanisms of the cardiovascular system in three-dimensional finite element models of arterial blood flow. *Ann Biomed Eng*. 2010;38:2314–2330. doi: 10.1007/s10439-010-9992-7
9. Vieira MS, Arthurs CJ, Hussain T, Razavi R, Figueroa CA. Patient-specific modeling of right coronary circulation vulnerability post-liver transplant in Alagille's syndrome. *PLoS One*. 2018;13:e0205829. doi: 10.1371/journal.pone.0205829
10. Yang W, Vignon-Clementel IE, Troianowski G, Reddy M, Feinstein JA, Marsden AL. Hepatic blood flow distribution and performance in conventional and novel Y-graft Fontan geometries: a case series computational fluid dynamics study. *J Thorac Cardiovasc Surg*. 2012;143:1086–1097. doi: 10.1016/j.jtcvs.2011.06.042
11. Baretta A, Corsini C, Yang W, Vignon-Clementel IE, Marsden AL, Feinstein JA, Hsia T-Y, Dubini G, Migliavacca F, Pennati G, et al. Virtual surgeries in patients with congenital heart disease: a multi-scale modelling test case. *Philos Trans R Soc A*. 2011;369:4316–4330. doi: 10.1098/rsta.2011.0130
12. Yang W, Feinstein JA, Vignon-Clementel IE. Adaptive outflow boundary conditions improve post-operative predictions after repair of peripheral pulmonary artery stenosis. *Biomech Model Mechanobiol*. 2016;15:1345–1353. doi: 10.1007/s10237-016-0766-5
13. Yang W, Hanley FL, Chan FP, Marsden AL, Vignon-Clementel IE, Feinstein JA. Computational simulation of postoperative pulmonary flow distribution in Alagille patients with peripheral pulmonary artery stenosis. *Congenit Heart Dis*. 2018;13:241–250. doi: 10.1111/chd.12556
14. Hacking WJ, VanBavel E, Spaan JA. Shear stress is not sufficient to control growth of vascular networks: a model study. *Am J Physiol*. 1996;270:H364–H375. doi: 10.1152/ajpheart.1996.270.1.H364
15. Pries AR, Secomb TW, Gaehtgens P. Structural adaptation and stability of microvascular networks: theory and simulations. *Am J Physiol*. 1998;275:H349–H360. doi: 10.1152/ajpheart.1998.275.2.H349
16. Pries AR, Reglin B, Secomb TW. Structural adaptation of microvascular networks: functional roles of adaptive responses. *Am J Physiol Heart Circ Physiol*. 2001;281:H1015–H1025. doi: 10.1152/ajpheart.2001.281.3.H1015
17. Carlson BE, Arciero JC, Secomb TW. Theoretical model of blood flow autoregulation: roles of myogenic, shear-dependent, and metabolic responses. *Am J Physiol Heart Circ Physiol*. 2008;295:H1572–H1579. doi: 10.1152/ajpheart.00262.2008
18. Updegrove A, Wilson NM, Merkow J, Lan H, Marsden AL, Shadden SC. SimVascular: an open source pipeline for cardiovascular simulation. *Ann Biomed Eng*. 2017;45:525–541. doi: 10.1007/s10439-016-1762-8
19. Taylor CA, Hughes TJR, Zarins CK. Finite element modeling of blood flow in arteries. *Comput Methods Appl Mech Eng*. 1998;158:155–196. doi: 10.1016/S0045-7825(98)80008-X
20. Jansen KE, Whiting CH, Hulbert GM. A generalized-α method for integrating the filtered Navier-Stokes equations with a stabilized finite element method. *Comput Methods Appl Mech Eng*. 2000;190:305–319. doi: 10.1016/S0045-7825(00)00203-6
21. Moghadam ME, Bazilevs Y, Hsia T-Y, Vignon-Clementel IE, Marsden AL. Modeling of Congenital Hearts Alliance (MOCHA). A comparison of outlet boundary treatments for prevention of backflow divergence with relevance to blood flow simulations. *Comput Mech*. 2011;48:277–291. doi: 10.1007/s00466-011-0599-0
22. Figueroa CA, Vignon-Clementel IE, Jansen KE, Hughes TJR, Taylor CA. A coupled momentum method for modeling blood flow in three-dimensional deformable arteries. *Comput Methods Appl Mech Eng*. 2006;195:5685–5706. doi: 10.1016/j.cma.2005.11.011
23. Moireau P, Xiao N, Astorino M, Figueroa CA, Chapelle D, Taylor CA, Gerbeau J-F. External tissue support and fluid-structure simulation in blood flows. *Biomech Model Mechanobiol*. 2012;11:1–18. doi: 10.1007/s10237-011-0289-z
24. Kobs RW, Muvarak NE, Eickhoff JC, Chesler NC. Linked mechanical and biological aspects of remodeling in mouse pulmonary arteries with hypoxia-induced hypertension. *Am J Physiol Heart Circ Physiol*. 2005;28:H1209–H1217. doi: 10.1152/ajpheart.01129.2003
25. Long CC, Hsu M-C, Bazilevs Y, Feinstein JA, Marsden AL. Fluid–structure interaction simulations of the Fontan procedure using variable wall properties. *Int J Numer Methods Biomed Eng*. 2012;28:513–527. doi: 10.1002/cnm.1485
26. Yang W, Dong M, Rabinovitch M, Chan FP, Marsden AL, Feinstein JA. Evolution of hemodynamic forces in the pulmonary tree with progressively worsening pulmonary arterial hypertension in pediatric patients. *Biomech Model Mechanobiol*. 2019;18:779–796. doi: 10.1007/s10237-018-01114-0
27. Moghadam ME, Vignon-Clementel IE, Figliola R, Marsden AL. A modular numerical method for implicit 0D/3D coupling in cardiovascular finite element simulations. *J Comput Phys*. 2013;244:63–79. doi: 10.1016/j.jcp.2012.07.035
28. Migliavacca F, Pennati G, Dubini G, Fumero R, Pietrabissa R, Urcelay G, Bove EL, Hsia T-Y, de Leval MR. Modeling of the Norwood circulation: effects of shunt size, vascular resistances, and heart rate. *Am J Physiol Heart Circ Physiol*. 2001;280:H2076–H2086. doi: 10.1152/ajpheart.2001.280.5.H2076
29. Pennati G, Migliavacca F, Dubini G, Pietrabissa R, de Leval MR. A mathematical model of circulation in the presence of the bidirectional cavopulmonary anastomosis in children with a univentricular heart. *Med Eng Phys*. 1997;19:223–234. doi: 10.1016/S1350-4533(96)00071-9
30. Mynard JP, Davidson MR, Penny DJ, Smolich JJ. A simple, versatile valve model for use in lumped parameter and one-dimensional cardiovascular models. *Int J Numer Methods Biomed Eng*. 2012;28:626–641. doi: 10.1002/cnm.1466
31. Tang BT, Fonte TA, Chan FP, Tsao PS, Feinstein JA, Taylor CA. Three-dimensional hemodynamics in the human pulmonary arteries under resting and exercise conditions. *Ann Biomed Eng*. 2011;39:347–358. doi: 10.1007/s10439-010-0124-1
32. Pennati G, Corsini C, Cosentino D, Hsia T-Y, Luisi VS, Dubini G, Migliavacca F. Boundary conditions of patient-specific fluid dynamics modelling of cavopulmonary connections: possible adaptation of pulmonary resistances results in a critical issue for a virtual surgical planning. *Interface Focus*. 2011;1:297–307. doi: 10.1098/rsfs.2010.0021
33. Tran JS, Schiavazzi DE, Ramachandra AB, Kahn AM, Marsden AL. Automated tuning for parameter identification and uncertainty quantification in multi-scale coronary simulations. *Comput Fluids*. 2017;142:128–138. doi: 10.1016/j.compfluid.2016.05.015
34. Tod ML, Sylvester JT. Distribution of pulmonary vascular pressure as a function of perinatal age in lambs. *J Appl Physiol*. 1989;66:79–87. doi: 10.1152/jappl.1989.66.1.79
35. Raj JU, Chen P. Micropuncture measurement of microvascular pressures in isolated lamb lungs during hypoxia. *Circ Res*. 1986;59:398–404. doi: 10.1161/01.RES.59.4.398
36. Eisenberg MC, Hayashi MAL. Determining identifiable parameter combinations using subset profiling. *Math Biosci*. 2014;256:116–126. doi: 10.1016/j.mbs.2014.08.008
37. Olufsen MS, Hill NA, Vaughan GDA, Sainsbury C, Johnson M. Rarefaction and blood pressure in systemic and pulmonary arteries. *J Fluid Mech*. 2012;705:280–305. doi: 10.1017/jfm.2012.220
38. Chambers MJ, Colebank MJ, Qureshi MU, Clipp R, Olufsen MS. Structural and hemodynamic properties of murine pulmonary

arterial networks under hypoxia-induced pulmonary hypertension. *Proc Inst Mech Eng H*. 2020;234:1312–1329. doi: 10.1177/0954411920944110
39. Pries AR, Neuhaus D, Gaehtgens P. Blood viscosity in tube flow: dependence on diameter and hematocrit. *Am J Physiol Heart Circ Physiol*. 1992;263:H1770–H1778. doi: 10.1152/ajpheart.1992.263.6.H1770
40. Secomb TW, Pries AR. Blood viscosity in microvessels: experiment and theory. *C R Phys*. 2013;14:470–478. doi: 10.1016/j.crhy.2013.04.002
41. Figueroa XF, Duling BR. Gap junctions in the control of vascular function. *Antioxid Redox Signal*. 2009;11:251–266. doi: 10.1089/ars.2008.2117
42. Antiga L, Piccinelli M, Botti L, Ene-Iordache B, Remuzzi A, Steinman DA. An image-based modeling framework for patient-specific computational hemodynamics. *Med Biol Eng Comput*. 2008;46:1097–1112. doi: 10.1007/s11517-008-0420-1
43. Guyton AC. The relationship of cardiac output and arterial pressure control. *Circulation*. 1981;64:1079–1088. doi: 10.1161/01.CIR.64.6.1079
44. Fleeter CM, Geraci G, Schiavazzi DE, Kahn AM, Marsden AL. Multilevel and multifidelity uncertainty quantification for cardiovascular hemodynamics. *Comput Methods Appl Mech Eng*. 2020;365:113030. doi: 10.1016/j.cma.2020.113030

SUPPLEMENTAL MATERIAL

Data S1. Supplemental Methods

Fluid-Structure Interaction Simulation

Hemodynamic simulations were performed with svSolver, SimVascular's finite element solver for the three-dimensional Navier-Stokes equations governing the flow of an incompressible and Newtonian fluid (19). Blood density and viscosity were respectively 1.06 g/ cm^3 and 0.04 g/(cm·s). The classical Streamline Upwind Petrov-Galerkin/pressure-stabilizing Petrov-Galerkin method was employed to stabilize the Galerkin formulation for spatial discretization, and the generalized-α method was employed for temporal discretization (20). Backflow stabilization was imposed via an additional convective traction with the parameter β fixed at 0.2 (21). Fluid-structure interaction was modeled with the coupled momentum method (22), which embeds a linear elastic membrane into the fluid problem on a single stationary mesh. To dampen non-physiological high-frequency wall oscillations, a Robin boundary condition representative of the viscoelastic Kelvin-Voigt model was prescribed on the wall as external tissue support. The spring and damping constants were respectively 10^3 g/(cm^2·s^2) and 10^4 g/(cm2.s) to reflect support found opposite to the spine (23).

Right Heart Lumped Parameter Network

The right ventricle (RV) was modeled as a chamber of varying elastance, such that the pressure was parameterized as follows by the end-systolic pressure volume relationship (ESPVR), end-diastolic pressure-volume relationship (EDPVR), and an activation function a representing progressive cardiac fiber excitation over a cardiac cycle T_c (26, 28, 29),

$$\frac{dV_{RV}}{dt} = Q_{TV} - Q_{PV} ,$$

$$P_{RV} = a\overline{\theta\ \mathrm{ESPVR}} + (1 - a)\ \mathrm{EDPVR} ,$$

$$a = \begin{cases} 2(1-k)\dfrac{t_m}{T_s} & t_m < \dfrac{T_s}{2}, \\ 1-k+k\sin\left[\pi\left(\dfrac{t_m}{T_s}-\dfrac{1}{2}\right)\right] & \dfrac{T_s}{2} \le t_m < T_s, \\ 1-\sin\left(\dfrac{\pi}{2}\dfrac{t_m-T_s}{T_r}\right) & T_s \le t_m < T_s+T_r, \\ 0 & t_m \ge T_s+T_r, \end{cases}$$

$$\text{ESPVR} = c_1 V_{RV} + c_2 ,$$

$$\text{EDPVR} = c_3 V_{RV} + c_4 ,$$

$$t_m = \text{mod}(t, T_c) ,$$

$$k = \frac{2}{\pi+2},$$

where V_{RV} is the RV volume, Q_{TV} and Q_{PV} are respectively the volumetric flow rates through the tricuspid (TV) and pulmonary valves (PV), T_s and T_r are respectively the durations of systole and isovolumetric relaxation, and θ, c_1, c_2, c_3, and c_4 are additional parameterization constants. Valve dynamics are modeled with dynamic pressure losses as a consequence of blood inertance and convective acceleration, parameterized with valve opening states ζ_{TV} and ζ_{PV} ranging between 0 (closed) and 1 (open) as follows,

$$L_{TV}\frac{dQ_{TV}}{dt} = P_{RA} - P_{RV} - \frac{\rho|Q_{TV}|}{2(A_{TV}\zeta_{TV})^2}Q_{TV} ,$$

$$L_{PV}\frac{dQ_{PV}}{dt} = P_{RV} - P_{MPA} - \frac{\rho|Q_{PV}|}{2(A_{PV}\zeta_{PV})^2}Q_{PV} ,$$

$$\frac{d\zeta_{TV}}{dt} = \begin{cases} (1-\zeta_{TV})K_{TV,o}(P_{RA}-P_{RV}) & P_{RA} \ge P_{RV} , \\ \zeta_{TV}K_{TV,c}(P_{RA}-P_{RV}) & P_{RA} < P_{RV} , \end{cases}$$

$$\frac{d\zeta_{PV}}{dt} = \begin{cases} (1-\zeta_{PV})K_{PV,o}(P_{RV}-P_{MPA}) & P_{RV} \ge P_{MPA} , \\ \zeta_{PV}K_{PV,c}(P_{RV}-P_{MPA}) & P_{RV} < P_{MPA} , \end{cases}$$

$$L_{TV} = \frac{\rho l_{TV}}{A_{TV}\zeta_{TV}},$$

$$L_{PV} = \frac{\rho l_{PV}}{A_{PV}\zeta_{PV}},$$

where L_{TV} and L_{PV} are the blood inertances through the valves, ρ is the density of blood, l_{TV} and l_{PV} are the effective valve lengths, A_{TV} and A_{PV} are the annulus areas, P_{RA} and P_{MPA} are respectively the right atrial (constant) and MPA pressures, $K_{TV,o}$ and $K_{PV,o}$ are the valve opening rate constants, and $K_{TV,c}$ and $K_{PV,c}$ are the valve closing rate constants (30). At each time step of the three-dimensional finite element solver, these ordinary differential equations were integrated with the fourth-order Runge-Kutta method.

Automated Tuning of Pre-Interventional Boundary Conditions

Each function evaluation of the high-fidelity zero-dimensional surrogate was solved using the generalized-α method and required a drastically reduced computational cost on the order of seconds, in contrast to the hours to days required for three-dimensional fluid-structure interaction simulations on high-performance computing clusters. Similarly to Tran et al. (33), numerical optimization of the zero-dimensional parameters was performed in two distinct stages following each three-dimensional simulation, such that the PA surrogate was first tuned to reflect simulated hemodynamics in the three-dimensional PA domain prior to tuning of the boundary conditions. In the first stage, all parameters in the inlet and outlet LPNs were kept fixed as we performed local Nelder-Mead optimization on the six parameters in the PA surrogate to achieve simulated systolic, diastolic, and mean MPA, RPA, and LPA pressures, spatially averaged over slices at their respective locations. In the second stage, the newly optimized surrogate parameters were kept fixed as we performed global optimization via the covariance matrix adaptation evolution strategy (CMA-ES) on parameters in the inlet and outlet LPNs to achieve clinically measured systolic, diastolic, and mean MPA, RPA, and LPA pressures. Pulmonary flow splits

weren't included as clinical targets, as lung perfusion scans aren't routinely performed for this patient cohort. The newly optimized resistances and capacitances for the aggregated Windkessel models were bilaterally distributed to the RPA and LPA outlets by cross-sectional area (12) prior to their use in the subsequent three-dimensional simulation. In both stages of optimization, the log barrier method was used to constrain degrees of freedom to physiological bounds. Specifically, the total downstream resistance and capacitance were constrained to 2.4×10^{2} dyn/cm^2 (or 3 Wood units) and 6.67×10^{-4} cm^5/dyn, respectively.

To ensure parameter identifiability with only 9 optimization targets but 35 degrees of freedom in the second stage of optimization (CMA-ES), the number of degrees of freedom were minimized through simplifications and assumptions. Given the unavailability of patient-specific inflow waveforms from MRA, the right heart LPN at the inlet was replaced with a prescribed healthy MPA inflow waveform (31) parameterized by two scaling factors governing the cardiac output and cardiac cycle duration. The log barrier method was again used to constrain both scaling factors to produce $\pm$20% of the clinically measured cardiac output and cardiac cycle duration. Upon conclusion of boundary condition tuning, parameters in the right heart LPN were separately optimized via the Nelder-Mead algorithm to achieve the tuned MPA inflow waveform. In addition, as suggested by lamb studies (34, 35), an equal distribution of PVR across the arterial, capillary, and venous compartments was assumed. Further assumptions include a 1:9 ratio between each pair of proximal and distal resistances in the Windkessel models, and equal capacitances in the capillary and venous compartments in each lung. Together, these assumptions reduced the number of degrees of freedom to just 8. For both the PA surrogate and boundary condition stages of optimization, parameter identifiability was verified by confirming invertibility of the Fisher Information Matrix (33, 36).

Autoregulatory Microvascular Adaptation

To model stable microvascular adaptation of the small PAs and arterioles, we adapted the following empirical model developed by Pries et al. (15, 16) to describe their experimental observations of topology and anatomy in rat mesentery microvascular networks,

$$\frac{dD}{dt} = \left(S_\tau + S_p + S_m + S_c + S_s\right)D \,,$$

$$S_\tau = \log(\tau_w + \tau_{\text{ref}}) \,,$$

$$S_p = -k_p \log(\tau_e) \,,$$

$$S_m = k_m \log\left(\frac{Q_{\text{ref}}}{QH_D} + 1\right),$$

$$S_c = k_c \frac{\tilde{S}_c}{\tilde{S}_c + S_0},$$

$$S_s = -k_s \,,$$

$$\tilde{S}_c = S_{m,a} + S_{m,b} + \tilde{S}_{c,a} \exp\left(\frac{-x_a}{L}\right) + \tilde{S}_{c,b} \exp\left(\frac{-x_b}{L}\right),$$

$$\tau_e = \frac{50}{86}\left[100 - 86 \exp(-5000 \log(\log(4.5P + 10))^{5.4}) - 14\right] + 1 \,,$$

where D is the diameter of a vessel segment in a structured tree; S_τ and S_p are the adaptive stimuli responsible for the opposing effects of wall shear stress τ_w and intraluminal pressure P; τ_{ref} is a small constant included to prevent singular behavior at low τ_w; and τ_e is the expected wall shear stress with a sigmoidal dependence on P, which we have scaled from the form in (15, 16) to represent typical ranges of distal PA pressures (< 20 mm Hg) and wall shear stress (< 50 dyn/cm^2) (26). S_m is the metabolic stimulus, which reflects adaptation in response to metabolic needs of the tissue perfused by the network and is a function of the actual and reference volumetric flow rates Q and Q_{ref} and discharge hematocrit $H_D = 0.45$; S_c is the conducted

stimulus representing upstream propagation of metabolic stimuli and therefore reflects the topological position of a vessel segment within the network; $\tilde{S}_c$ is the conducted stimulus at a given junction, with contributions from the metabolic and conducted stimuli of the two downstream daughter segments, denoted by a and b; and S_0 is a reference sum imparting a nonlinear saturable response. The conducted signals are assumed to decay exponentially with distance traveled, where x_a and x_b are the daughter segment lengths, and L is a length constant. Finally, S_s is the shrinking tendency that reflects the tendency for segments to collapse in the absence of positive growth stimuli; and k_p, k_m, k_c, and k_s are the relevant sensitivity parameters.

In order to determine the 8 adaptive parameters specific to PA microvasculature, we leveraged Nelder-Mead optimization to identify parameters that yielded the most stable networks under adaptation with pre-interventional hemodynamics. For each patient, upon completion of the *pre-interventional simulation*, a temporary structured tree was generated for each three-dimensional PA outlet with a tree root diameter equal to that of the three-dimensional outlet. Recursive bifurcation was carried out with diameter scaling factors of $\alpha = 0.9$ and $\beta = 0.58$ until termination at the minimum diameter $D_{\text{min}} = 0.005$ cm (37, 38). Each vessel segment was prescribed a length in mm of $x = 12.4r^{1.1}$, where r is the radius in mm (37). Given the time-averaged simulated pre-interventional outflows, every function evaluation consisted of adapting diameters of all vessel segments across all structured trees via explicit Euler time integration, in which the Poiseuille assumption was applied at every time step to solve for P, Q, and τ_w at segment inlets. The Fåhraeus-Lindqvist effect was modeled with Pries et al.'s empirical description of in vivo apparent viscosity μ_{app} relative to plasma viscosity $\mu_{\text{plasma}} = 1.2 \times 10^{-2}$ poise (39, 40),

$$\frac{\mu_{\text{app}}}{\mu_{\text{plasma}}} = \left[1 + (\mu_{0.45}^{*} - 1)\frac{(1 - H_D)^C - 1}{(1 - 0.45)^C - 1}\left(\frac{D}{D - 1.1}\right)^2\right]\left(\frac{D}{D - 1.1}\right)^2,$$

$$\mu_{0.45}^{*} = 6\exp(-0.085D) + 3.2 - 2.44\exp(-0.06D^{0.645}),$$

$$C = \big(0.8 + \exp(-0.075D)\big)(-1 + (1 + 10^{-11}D^{12})^{-1}) + (1 + 10^{-11}D^{12})^{-1}.$$

Segments with diameters that fell under D_{min} were considered to have collapsed and were thus immediately pruned from the trees. Squared differences between the initial and adapted diameters were summed over all segments for the objective function. Optimized parameters were averaged across all patients and used for all subsequent structured tree adaptations: sensitivity to intraluminal pressure $k_p = 1.24$, sensitivity to metabolic stimuli $k_m = 2.29 \times 10^{-1}$, sensitivity to conducted stimuli $k_c = 2.20$, basal shrinking rate $k_s = 8.85 \times 10^{-1}$, reference wall shear stress $\tau_{\text{ref}} = 2.19 \times 10^{-1}$ dyn/cm^2, reference volumetric flow rate $Q_{\text{ref}} = 9.66 \times 10^{-7}$ cm^3/s, reference length $L = 1.9974$ cm, and reference sum of conducted stimuli $S_0 = 5.9764 \times 10^{-4}$. These parameters yielded structured trees of stable topology upon adaptation with pre-interventional hemodynamics. While most of these identified parameters fell within the same order of magnitude as parameters identified by Pries et al. for rat mesentery microvasculature, S_0 was noticeably different compared to their value of 20. S_0 regulates the saturation of the conducted response in the upstream direction from the capillaries to arterioles, which is thought to occur via electrotonic conduction of changes in membrane potential through gap junctions between smooth muscle cells and endothelial cells (41). The small magnitude of our PPAS-specific S_0 effectively eliminated the saturation response, suggesting a much larger role for conduction of vasomotor responses in the human pulmonary vasculature as compared to the rat mesentery vasculature.

For each outlet, we generated a *pre-interventional baseline structured tree* that was consistent with the tuned pre-interventional arterial resistance (the sum of the proximal and distal resistances in the arterial Windkessel model) found in the automated tuning framework described above. Specifically, we again used Nelder-Mead optimization to identify the tree root radius that best achieved the tuned pre-interventional arterial resistance upon stable adaptation with pre-interventional hemodynamics. With the Poiseuille assumption, structured tree resistances were computed upstream by summing segment resistances in series and parallel according to the structured tree topologies.

To determine flow perturbations solely due to a transcatheter intervention, an *intermediate simulation* was performed on each post-interventional anatomy with the pre-interventional boundary conditions. Outflows from the intermediate simulation were then used to adapt the pre-interventional baseline structured trees. The resistance of each adapted tree was computed upstream and prescribed as the adapted downstream arterial resistance for the *post-interventional simulation* with the assumption of a 1:9 ratio between the proximal and distal resistances.

Table S1. Pre- and post-interventional target and simulated hemodynamics.

Patient	Target / Simulation	P_{MPA} (mm Hg)	P_{RPA} (mm Hg)	P_{LPA} (mm Hg)	CO (L/min)	Flow Split (% Right)
AS-1	**Pre Target**	**90 / 18 m42**	**50 / 18 m32**	**50 / 18 m32**	**5.84**	**52% R**
	Pre	94.1 / 20.4 m43.0	45.6 / 20.1 m28.8	53.5 / 20.2 m32.3	5.19	54.7% R
	Prox	95.4 / 20.4 m42.9	48.2 / 20.1 m29.3	86.1 / 20.1 m40.4	5.21	54.0% R
	Extv Target	**59 / 13 m29**	**N/A**	**57 / 13 m29**	**N/A**	**N/A**
	Extv	55.4 / 20.4 m31.8	40.0 / 20.2 m27.4	52.8 / 20.2 m30.6	5.43	74.9% R
AS-2	**Pre Target**	**100 / 6 mN/A**	**11 / 6 m8**	**18 / 10 m11**	**1.07**	**N/A**
	Pre	97.9 / 6.38 m28.0	11.4 / 6.09 m7.84	18.3 / 5.83 m9.31	1.14	38.6% R
	Prox Target	**71 / 8 mN/A**	**N/A**	**N/A**	**N/A**	**N/A**
	Prox	70.3 / 6.89 m23.0	56.5 / 6.86 m19.7	50.6 / 6.62 m18.0	1.34	41.3% R
	Extv	43.9 / 7.56 m17.8	25.7 / 7.59 m13.0	22.9 / 7.03 m12.0	1,64	46.6% R
AS-3	**Pre Target**	**68 / 15 m38**	**39 / 12 m22**	**29 / 15 m21**	**2.60**	**68% R**
	Pre	70.2 / 17.3 m33.5	41.1 / 17.3 m25.4	29.6 / 17.3 m21.9	2.48	66.9% R
	Prox	55.0 / 17.3 m28.8	44.3 / 17.2 m25.8	44.7 / 17.2 m26.0	2.58	59.1% R

	Extv	43.2 / 17.3 m25.4	29.7 / 17.2 m21.8	33.2 / 17.2 m22.5	2.72	66.5% R
AS-4	**Pre Target**	**50 / 11 m26**	**37 / 11 m23**	**18 / 8 m13**	**2.69**	**56% R**
	Pre	49.6 / 10.1 m23.8	33.5 / 9.70 m18.7	22.0 / 10.0 m14.8	2.65	59.9% R
	Prox	47.9 / 10.5 m23.4	33.2 / 10.0 m18.7	33.5 / 10.2 m18.5	2.69	58.0% R
	Extv	34.2 / 11.1 m19.1	29.0 / 10.8 m17.3	13.2 / 10.8 m12.1	2.89	53.4% R
WS-1	**Pre Target**	**125 / 21 mN/A**	**19 / 11 m15**	**27 / 21 m25**	**1.22**	**N/A**
	Pre	126 / 16.5 m49.3	20.9 / 15.3 m17.2	31.0 / 16.6 m21.0	1.29	56.1% R
	Prox	117 / 16.4 m45.5	34.5 / 15.9 m22.0	40.0 / 16.5 m23.7	1.43	52.5% R
	Extv	114 / 17.2 m44.6	20.7 / 16.2 m17.9	20.7 / 5.63 m16.7	1.50	50.6% R
WS-2	**Pre Target**	**93 / 16 m42**	**20 / 10 m17**	**27 / 21 m25**	**1.02**	**N/A**
	Pre	93.9 / 14.6 m37.9	22.9 / 14.7 m17.6	25.6 / 13.0 m17.0	1.16	53.3% R
	Prox	69.0 / 14.9 m31.0	35.7 / 14.8 m21.9	58.5 / 14.4 m27.3	1.51	48.7% R
	Extv	55.3 / 14.6 m27.0	24.0 / 14.6 m18.3	28.0 / 14.0 m18.9	1.70	41.2% R

AS: Alagille Syndrome. WS: Williams Syndrome. P_{MPA}, P_{RPA}, P_{LPA}: main, central right, and central left pulmonary artery (MPA, RPA, LPA) pressures (systolic/diastolic and mean (m)). CO: cardiac output. Pre: pre-intervention. Prox: proximal intervention. Extv: extensive intervention. N/A: not available.